

1 Retrieval of Solar-induced Chlorophyll Fluorescence from Satellite

2 Measurements: Comparison of SIF between TanSat and OCO-2

3 Lu Yao¹, Yi Liu¹, Dongxu Yang¹, Zhaonan Cai¹, Jing Wang¹, Chao Lin², Naimeng Lu³, Daren Lyu¹,
4 Longfei Tian⁴, Maohua Wang⁵, Zengshan Yin⁴, Yuquan Zheng², Sisi Wang⁶

6 ¹Carbon Neutral Research Center & Key Laboratory of Middle Atmosphere and Global Environment Observation, Institute of
7 Atmospheric Physics, Chinese Academy of Sciences, No. 40, Huayan Li, Chaoyang District, Beijing 100029, China

8 ²Changchun Institute of Optics, Fine Mechanics and Physics, Changchun 130033, China

9 ³National Satellite Meteorological Center, China Meteorological Administration, Beijing 100081, China

10 ⁴Shanghai Engineering Center for Microsatellites, Shanghai 201203, China

11 ⁵Shanghai Advanced Research Institute, Chinese Academy of Sciences, Shanghai 201210, China

12 ⁶National Remote Sensing Center of China, Beijing 100036, China

16 Correspondence to: Dongxu Yang (yangdx@mail.iap.ac.cn)

17 **Abstract.** Solar-induced chlorophyll fluorescence (SIF) is emitted during photosynthesis in plant leaves. It constitutes a small
18 additional offset to reflected radiance and can be observed by sensitive instruments with high signal-to-noise ratio and spectral
19 resolution. The Chinese global carbon dioxide monitoring satellite (TanSat) acquires measurements of greenhouse gas column
20 densities. The advanced technical characteristics of the grating spectrometer (ACGS) onboard TanSat enable SIF retrievals
21 from observations in the O₂-A band. In this study, one year of SIF data was retrieved from Orbiting Carbon Observatory-2
22 (OCO-2) and TanSat measurements using the IAPCAS/SIF algorithm. A comparison between the IAPCAS/SIF results
23 retrieved from OCO-2 spectra and the official OCO-2 SIF product (OCO2_Level 2_Lite_SIF.8r) shows a strong linear
24 relationship ($R^2 > 0.85$) and suggests good reliability of the IAPCAS/SIF retrieval algorithm. Comparing global distributions
25 of SIF retrieved by IAPCAS/SIF from TanSat and OCO-2 shows the same spatial pattern for all seasons with gridded SIF
26 difference less than $0.3 \text{ W m}^{-2} \mu\text{m}^{-1} \text{ sr}^{-1}$. The global distributions also agree well with the official OCO-2 SIF product with
27 difference less than $0.2 \text{ W m}^{-2} \mu\text{m}^{-1} \text{ sr}^{-1}$. The retrieval uncertainty of seasonally gridded TanSat IAPCAS/SIF is less than 0.03
28 $\text{W m}^{-2} \mu\text{m}^{-1} \text{ sr}^{-1}$ whereas the uncertainty of each sounding ranges from 0.1 to $0.6 \text{ W m}^{-2} \mu\text{m}^{-1} \text{ sr}^{-1}$. The relationship between
29 annually-averaged SIF products and FLUXCOM gross primary productivity (GPP) was also estimated for six vegetation types
30 in a $1^\circ \times 1^\circ$ grid over the globe, indicating that the SIF data from the two satellites have the same potential in quantitatively
31 characterizing ecosystem productivity. The spatiotemporal consistency between TanSat and OCO-2 and their comparable data
32 quality enable joint usage of the two mission products. Data supplemented by TanSat observations are expected to contribute
33 to the development of global SIF maps with more spatiotemporal detail, which will advance global research on vegetation
34 photosynthesis.

删除的内容: 1

删除的内容: 1

带格式的: 突出显示

删除的内容: 1

带格式的: 突出显示

带格式的: 突出显示

删除的内容: Lin²...in², Naimeng Lu³...u³, Daren Lyu¹, Longfei
Tian⁴...ian⁴, Maohua Wang⁵...ang⁵, Zengshan Yin⁴...in⁴, Yuquan
Zheng²...heng², Sisi Wang⁶

带格式的

删除的内容: ²University of Chinese Academy of Sciences, No. 19A,
Yuquan Lu, Shijing Shan District, Beijing 100049, China
³Shanghai Advanced Research Institute, Chinese Academy of
Sciences, Shanghai 201210, China
⁴Changchun

带格式的

删除的内容: ⁵National

删除的内容: ⁶Shanghai

已下移 [1]: ⁷National Remote Sensing Center of China, Beijing
100036, China

带格式的: 非突出显示

已移动 (插入) [1]

删除的内容: ⁷

删除的内容: that ...ith high signal-to-noise ratio and spectral
resolution. The Chinese global carbon dioxide monitoring satellite
(TanSat), as its mission, ...acquires measurements of greenhouse gas
column densitiesgreenhouse gas column density... The advanced
technical characteristics of the hyper-spectrum ...rating spectrometer
(ACGS) onboard TanSat enable SIF retrievals from
space ...bservations in the O₂-A band. In this study, one ...ear of
SIF data for each sounding

带格式的: 突出显示

删除的内容: their ... strong linear relationship ($R^2 > 0.85$) and
suggests the ...ood reliability of the IAPCAS/SIF retrieval algorithm.
Comparing global distributions of SIF retrieved by IAPCAS/SIF
from TanSat and OCO-2 shows The global distribution showed that
the SIF retrieved from the two satellites shared ...he same spatial
pattern for all seasons with the

删除的内容: ... The global distributions also agreed and they also
agreed ...well with the official OCO-2 SIF product with the

删除的内容: -

删除的内容: make the comprehensive usage of the two mission
products possible.

108 **1 Introduction**

109 Terrestrial vegetation ecosystems play a large role in the global carbon cycle through the processes of photosynthesis and
110 respiration. Incoming radiation is absorbed, reflected, and/or transmitted by plant leaves. A portion of the absorbed radiation
111 is used by the chlorophyll in plant leaves for carbon fixation, while the rest is either dissipated as heat or re-emitted as solar-
112 induced chlorophyll fluorescence (SIF) at longer wavelengths (Frankenberg et al., 2011a, 2014). In contrast to the traditional
113 remotely sensed vegetation indices obtained from some studies (Frankenberg et al., 2011b; Guanter et al., 2014; Li et al., 2018;
114 Sun et al., 2017a; Yang et al., 2015; Zhang et al., 2014), SIF offers the potential to measure photosynthetic activity and gross
115 primary production (GPP), due to the strong correlation between these measures (Frankenberg et al., 2011b; Guanter et al.,
116 2012, 2014). The fluorescence emission adds a low-intensity radiance of less than $10 \text{ W m}^{-2} \mu\text{m}^{-1} \text{ sr}^{-1}$ and fills in the solar
117 absorption features of the reflected spectrum (Frankenberg et al., 2011a). The filling-in effect of the solar lines (Fraunhofer
118 lines) is the basic principle applied to measure SIF from space using the capabilities of hyperspectral observation (Frankenberg
119 et al., 2011b; Guanter et al., 2012).

120 The first attempt of observing SIF from space was performed using images acquired by the Medium Resolution Imaging
121 Spectrometer (MERIS) onboard the ENVIRONMENTAL SATellite (ENVISAT) (Guanter et al., 2007). This led to a new idea for
122 conducting SIF studies on a global scale. The first global SIF map was retrieved from high-resolution spectra of the
123 Greenhouse-gases Observing SATellite (GOSAT) (Joiner et al., 2011; Frankenberg et al., 2011b). After that, SIF retrievals
124 were implemented for a variety of satellite measurements, such as those from the Global Ozone Monitoring Experiment-2
125 (GOME-2) instruments onboard meteorological operational satellites, SCIAMACHY onboard ENVISAT, and Orbiting
126 Carbon Observatory-2 (OCO-2) (Joiner et al., 2016; Köhler et al., 2015). The TROPOspheric Monitoring Instrument
127 (TROPOMI) onboard Sentinel 5 Precursor (S-5P) provides more efficient SIF observations in terms of global coverage and
128 new opportunities for exploring the application potential of SIF data in the terrestrial biosphere as well as in climate research
129 (Doughty et al., 2019; Köhler et al., 2018b). Furthermore, an upcoming European Space Agency mission called FLuorescence
130 EXplorer (FLEX), the first satellite dedicated to SIF observation, will launch in the middle of 2024 (Drusch et al., 2017). Many
131 studies on SIF applications have been initiated with the accumulation of SIF products in recent years. The responses of satellite-
132 measured SIF to environmental conditions have been applied to drought dynamics monitoring and regional vegetation water
133 stress estimation (Lee et al., 2013; Sun et al., 2015; Yoshida et al., 2015). As a proxy of photosynthesis, SIF acts as a powerful
134 constraint parameter in estimating carbon exchange in an ecosystem between the atmosphere, ocean, and soil; as such, the
135 analysis of the relationship between SIF and GPP has become an important research topic (Li et al., 2018; Köhler et al., 2018a;
136 Sun et al., 2017a; Zhang et al., 2018). The strong linear relationship between them paves the way for improving terrestrial
137 ecosystem model simulations of GPP, along with consequent improvement of global carbon flux estimation (MacBean et al.,
138 2018; Yin et al., 2020). GPP estimations based on satellite-measured SIF have proven to be an effective method validated by
139 in-situ flux observations (Joiner et al., 2018; Qiu et al., 2020). However, uncertainty in the factors that determine the
140 relationship between SIF and GPP still exists and is a key limitation in the application of SIF to flux estimation. Based on

删除的内容: Terrestrial vegetation accounts for a large part of the ecosystem, with its photosynthesis and respiration processes playing important roles in the global carbon cycle

删除的内容: photosynthesis

删除的内容: (Fs)

删除的内容: at

删除的内容: research based on space-based observations

删除的内容: with

删除的内容: from

删除的内容: from

删除的内容:

删除的内容:

删除的内容: emission

154 multi-satellite SIF products, eddy covariance flux tower observations, and ecological models, the relationship between SIF and
155 GPP under different environmental conditions has been discussed in a number of studies to analyze the dominant factors for
156 the growing status of different biomes, such as temperature, soil moisture, and vegetation types (Chen et al., 2020; Doughty et
157 al., 2019; Li et al., 2020; Qiu et al., 2020; Yin et al., 2020).

158 The Chinese global carbon dioxide monitoring satellite (TanSat) was launched in December 2016. Aiming at acquiring CO₂
159 concentrations similar to OCO-2, TanSat flies in a sun-synchronous orbit at approximately 700 km height with a 16-day repeat
160 cycle and an equator crossing time of ~1:30 p.m. local time (Cai et al., 2014; Liu et al., 2018; Yang et al., 2018). Onboard
161 TanSat, the hyperspectral Atmospheric Carbon-dioxide Grating Spectrometer (ACGS) is designed to separately record solar
162 backscatter spectra in three channels centered at 0.76 μm (O₂-A band), 1.61 μm (weak CO₂ absorption band), and 2.06 μm
163 (strong CO₂ absorption band). Many Optimal Estimation Method (OEM) full physics retrieval algorithms have been developed
164 and applied for the total column-averaged dry air CO₂ mole fraction (XCO₂) retrievals (Bösch et al., 2006; O'Dell et al., 2012;
165 Reuter et al., 2010; Yang et al., 2015b; Yoshida et al., 2011, 2013). The Institute of Atmospheric Physics Carbon Dioxide
166 Retrieval Algorithm for Satellite Remote Sensing (IAPCAS) algorithm has been applied for TanSat XCO₂ retrievals (Yang et
167 al., 2018; Yang et al., 2021) and was also previously tested on spectra from the GOSAT and OCO-2 missions (Yang et al.,
168 2015b). However, the fluorescence feature causes substantial biases when retrieving surface pressure and scattering parameters
169 from the O₂-A band, and the associated errors propagate into the XCO₂ retrievals. In previous XCO₂ retrievals, the surface
170 emissions were well modeled as a continuum offset of the O₂-A band to reduce errors (Frankenberg et al., 2011a, 2012; Joiner
171 et al., 2012). For TanSat, its high spectral resolution of ~0.044 nm and a signal-to-noise ratio of ~360 in the O₂-A band makes
172 it possible to obtain SIF, with a spatial resolution of 2 km × 2 km in nadir mode (Liu et al., 2018).

173 Various approaches have been used to infer SIF from satellite measurements (Frankenberg et al., 2011b, 2014a, 2014b; Guanter
174 et al., 2007, 2012, 2015; Joiner et al., 2011, 2013, 2016; Köhler et al., 2015, 2018b). The SIF signal induces a filling-in effect
175 of solar lines, which can be used for SIF retrieval, as the fractional depth of solar Fraunhofer lines does not change during
176 radiation transmission in the atmosphere. To be able to measure the filling-in features from SIF, high-resolution spectra are
177 required to describe subtle changes in the spectral absorption lines. Given highly resolved spectral features, a method was
178 developed based on solar line fitting and the Beer-Lambertian law. This method is robust and accurate when the spectrum is
179 out of the influence of telluric absorptions, even in the presence of aerosols (Frankenberg et al., 2011a; Joiner et al., 2011); in
180 the current study, this method was applied to develop the IAPCAS/SIF algorithm. Another SIF retrieval method is the data-
181 driven algorithm based on the singular value decomposition (SVD) technique (Joiner et al., 2011; Guanter et al., 2012), which
182 has been broadly applied to GOSAT, OCO-2, TanSat and TROPOMI (Joiner et al., 2011; Guanter et al., 2012, 2015;
183 Frankenberg et al., 2014a; Du et al., 2018; Köhler et al., 2018b). In the data-driven method, the spectrum is represented as a
184 linear combination of the SIF signal and several singular vectors that are trained from non-fluorescent scenes by SVD; thus,
185 the SIF signal can be obtained with linear least-squares fitting (Du et al., 2018; Guanter et al., 2012). The first TanSat SIF
186 map was obtained by the SVD method (Du et al., 2018). In a previous study, a new TanSat SIF product retrieved by
187 IAPCAS/SIF algorithm was introduced and the two kinds of TanSat SIF products by IAPCAS/SIF and the SVD methods were

刪除的內容: as

刪除的內容: in

刪除的內容: With the recorded spectra, m

刪除的內容:

刪除的內容: Boesche

刪除的內容: 2009

刪除的內容: Butz et al., 2009, 2011;

刪除的內容: zero

刪除的內容: Butz et al., 2009, 2010;

刪除的內容: The

刪除的內容: from space measurements

刪除的內容: recognize

刪除的內容: by

刪除的內容: and an instrument spectral response function (ISRF)

刪除的內容: With

刪除的內容: the detailed

刪除的內容: in

刪除的內容: SIF retrieval

206 compared (Yao et al., 2021). The preliminary comparison between the two TanSat SIF products showed that the two SIF
 207 products share a similar global pattern and signal magnitude for all seasons while different biases still exist in four seasons
 208 (Yao et al., 2021). The different biases in the four seasons may be caused by the different training samples of the SVD method,
 209 which indicates that the training samples have a significant impact on the retrieval results. In order to obtain stable SIF data
 210 products from TanSat and other subsequent satellite missions, it is particularly important to establish a stable and high-
 211 precision SIF inversion algorithm. To further validate the IAPCAS/SIF algorithm and to test the potential for synergistic,
 212 multi-satellite SIF analysis, in this study, we detail the IAPCAS/SIF algorithm for TanSat and we compare the SIF products
 213 from TanSat and OCO-2 for a range of spatiotemporal scales.

删除的内容: shows

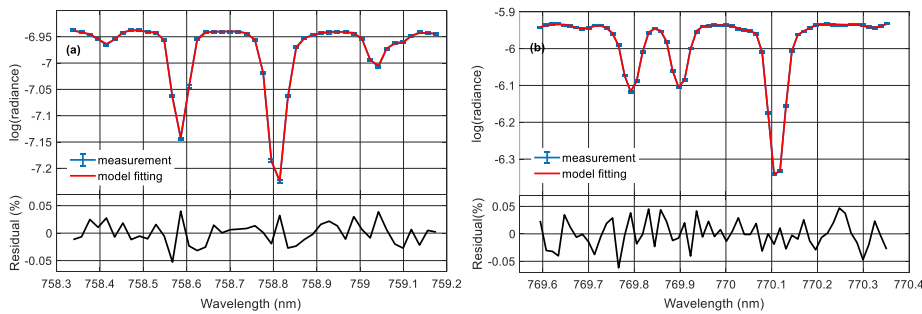
删除的内容: To detailed validate the IAPCAS/SIF algorithm and test the potential of comprehensive usage of multi-satellites SIF data in analysis, in this study, we detailed the TanSat SIF retrieval using the IAPCAS/SIF algorithm and made a comparison of SIF products between TanSat and OCO-2 in variety of temporal-spatial scales, although a preliminary test was shown in previous work.

214 2 Data and retrieval algorithm

215 2.1 Retrieval Principle and Method

216 We used TanSat version 2 Level 1B (L1B) nadir-mode earth observation data in the retrieval process. The measurements
 217 covered the period from March 2017 to February 2018. Polarized radiance in the O₂-A band with a spectral resolution of 0.044
 218 nm was provided in the L1B data, and two micro-windows near 757 nm (758.3-759.2 nm) and 771 nm (769.6-770.3 nm) were
 219 chosen to retrieve top-of-atmosphere (TOA) SIF while avoiding the contamination from strong lines of atmospheric gas
 220 absorption. The retrieval was independent for each micro-window as shown in Figure 1. To avoid duplication of information,
 221 we use the SIF product at 757 nm as the example in the analysis.

删除的内容: the



223 **Figure 1: The fitted spectra and residuals for the (a) 757 nm and (b) 771 nm micro-windows of TanSat measurement. The error bar**
 224 **of the measured spectra depicts the estimated precision of each TanSat sounding.**

225

226 Filling-in on solar lines by chlorophyll fluorescence in the O₂-A band can be detected in the hyperspectral measurements from
 227 TanSat. This effect on spectral radiance is different from the impact of atmospheric and surface processes, e.g., scattering and
 228 absorption. For example, scattering by aerosols and clouds does not change the relative depth of clear solar lines, unlike the

237 SIF emission signal. We applied the differential optical absorption spectroscopy (DOAS) technique to IAPCAS/SIF algorithm
 238 for TanSat measurement (Frankenberg, 2014b; Sun et al., 2018).

239 The TOA spectral radiance (L_{TOA}^λ) at wavelength λ can be represented as follows:

$$240 L_{TOA}^\lambda = I_t^\lambda \cdot \mu_0 \cdot \left(\rho_0^\lambda + \frac{\rho_s^\lambda \cdot T_1^\lambda \cdot T_2^\lambda}{\pi} \right) + F_{TOA}^\lambda \quad (1)$$

241 where I_t^λ is the incident solar irradiance at the TOA, μ_0 is the cosine of the solar zenith angle (SZA), ρ_0^λ is atmospheric path
 242 reflectance, ρ_s^λ is surface reflectance, and T_1^λ and T_2^λ are the total atmospheric transmittances along the light-path in the
 243 downstream and upstream directions, respectively. F_{TOA}^λ is the SIF radiance at TOA.

244 The first term on the right of Eq. (1) represents the transmission process of solar radiance. In the micro-windows used in SIF
 245 retrieval, gas absorption is very weak and smooth, and hence, the atmosphere term $\mu_0 \cdot \left(\rho_0^\lambda + \frac{\rho_s^\lambda \cdot T_1^\lambda \cdot T_2^\lambda}{\pi} \right)$ can be simplified to a
 246 low-order polynomial $\sum_{i=0}^n a_i \cdot \lambda^i$ that varies with λ (Joiner et al., 2013; Sun et al., 2018); this is always valid as long as the
 247 spectrum fitting range is out of sharp atmospheric absorptions. Then Eq. (1) could be represented as:

$$248 L_{TOA}^\lambda(F_{TOA}^\lambda, \mathbf{a}) = \langle I_t^\lambda \rangle * \sum_{i=0}^n a_i \cdot \lambda^i + F_{TOA}^\lambda \quad (2)$$

249 where $\langle \rangle$ denote the convolution with the ISRF from line-by-line spectra, and the coefficient vector \mathbf{a} determines the
 250 wavelength dependence polynomial for the atmosphere term.

251 To facilitate the extraction of SIF signals, the radiance is normalized to the continuum level radiance and the relative
 252 contribution of SIF to the continuum level radiance F_s^{rel} is defined. In the micro-window, SIF was regarded as a constant signal
 253 due to its small changes. When the spectral radiance measurement was converted to logarithmic space, the forward model was
 254 expressed as:

$$255 f(F_s^{rel}, \mathbf{b}) = \log(\langle I_t + F_s^{rel} \rangle) + \sum_{i=0}^n b_i \cdot \lambda^i \quad (3)$$

256 Where J_t is a normalized disk-integrated solar transmission model. The vector \mathbf{b} consists of the polynomial coefficients b_i
 257 and we used a second-order polynomial ($i = 0, 1, 2$) in the retrieval.

258 Although the atmospheric gas absorption was very weak in the micro-window, the weak absorption and the far-wing effects
 259 (O₂ lines) can still change spectral features, which induces errors in spectrum fitting. In other physics-based retrievals, the
 260 surface pressure data of the European Centre for Medium-Range Weather Forecasts (ECMWF) together with topographic data
 261 are usually used as the true surface pressure to simulate the atmospheric transmission in the range of the O₂-A band. However,
 262 there is still a difference between the true surface pressure and the model surface pressure, so we introduced a factor here to
 263 reduce the influence of the inaccurate surface pressure. In the IAPCAS/SIF algorithm, we use the ECMWF interim surface
 264 pressure (0.75° × 0.75°) to estimate O₂ absorption first, and then modify the absorption feature by a scale factor. The scale
 265 factor is obtained simultaneously in SIF retrieval to reduce the error induced by the uncertainty in surface pressure. As
 266 described by Yang (2020), there is also a continuum feature in TanSat L1B data that needs to be considered for the high-quality
 267 fitting of the O₂-A band. However, in this study, this continuum feature was not corrected, as the impact of such a smooth

- 带格式的: 非突出显示
- 带格式的: 非突出显示
- 带格式的: 非突出显示
- 带格式的: 非突出显示
- 带格式的: 字体: (中文) Times New Roman, 非突出显示
- 带格式的: 字体: (中文) Times New Roman
- 带格式的: 非突出显示
- 带格式的: 非突出显示
- 带格式的: 非突出显示
- 带格式的: 非突出显示
- 带格式的: 非突出显示
- 带格式的: 非突出显示
- 带格式的: 非突出显示
- 已移动(插入) [2]
- 删除的内容: In the retrieval, the spectral radiance measurement was converted to logarithmic space by the instrument and the radiative transfer process $f(F_s^{rel}, \mathbf{a})$ was represented as follows: $f(F_s^{rel}, \mathbf{a}) = \log(\langle I_t + F_s^{rel} \rangle) + \sum_{i=0}^n a_i \cdot \lambda^i$ (2).
- where $\langle \rangle$ denote the convolution with the ISRF from line-by-line spectra.
- 带格式的: 非突出显示
- 带格式的: 非突出显示
- 带格式的: 非突出显示
- 带格式的: 非突出显示
- 删除的内容: polynomial coefficient
- 删除的内容: \mathbf{a}
- 带格式的: 非突出显示
- 删除的内容: determines
- 删除的内容: the wavelength dependence polynomial for the atmosphere term; in the retrieval, we used a second-order polynomial
- 已上移 [2]: I_t is a normalized disk-integrated solar transmission
- 带格式的: 非突出显示
- 带格式的: 非突出显示
- 删除的内容: physical
- 删除的内容: is
- 带格式的: 下标
- 删除的内容: simulate the molecular absorption cross-section
- 删除的内容: t
- 删除的内容: d
- 删除的内容: ly
- 删除的内容: modified

296 continuum variation in the micro-window is weak and the polynomial continuum model is capable of compensating for most
297 of this effect.

298 The state vector includes the relative SIF signal F_s^{rel} , a wavenumber shift, the scale factor for the O_2 column absorption, and
299 coefficients of the polynomial. The continuum level radiance I_{cont} within the fitting window is calculated using the radiance
300 outside the absorption features in the micro-window and is then used for the actual SIF signal calculation thus: $F = F_s^{rel} \cdot I_{cont}$.

301 In the IAPCAS/SIF algorithm, we used an OEM for state vector optimization in the retrieval process. Compared to the IAPCAS
302 XCO₂ retrieval, the IAPCAS/SIF retrieval employs a state vector with fewer elements and a much simpler forward model, so
303 there is no need to perform complex radiative transfer calculations. Considering the low complexity of SIF retrieval, the Gauss-
304 Newton method was applied iteratively to find the optimal solution.

305 2.2 Bias Corrections

306 A systematic error remains in the raw SIF retrieval output if no bias correction is performed; similar results have been reported
307 in GOSAT and OCO-2 SIF retrieval studies (Frankenberg et al., 2011a, 2011b; Sun et al., 2018). This is because the SIF signal
308 is weak (e.g., typically ~1-2% of the continuum level radiance), which means that even a small issue in the measurement, such
309 as a zero-offset caused by radiometric calibration error, could induce significant bias. Unfortunately, the lack of knowledge on
310 in-flight instrument performance makes it difficult to perform a direct systematic bias correction in the measured spectrum.

311 The bias was considered to be related to the continuum level radiance in the previous works. To get the relationship between
312 the continuum level radiance and the bias, we calculated the mean bias for continuum level radiance at the interval of 5 W m^{-2}
313 $\mu\text{m}^{-1} \text{ sr}^{-1}$ from all non-fluorescence measurements, and then a piecewise linear function fit was applied to describe the
314 relationship between the continuum level radiance and the biases.

315 The non-fluorescence soundings that were used in the bias estimation were based on the dataset “sounding_landCover” in
316 TanSat L1B data. This dataset depends on the MODIS land cover product and provides a scheme consisting of 17 land cover
317 classifications defined by the International Geosphere-Biosphere Programme. The measurements marked as “snow and ice,”
318 “barren,” and “sparsely vegetated” were chosen to estimate the bias. Calibrations compensated for most of the instrument
319 degradations, but this alone was not perfect. To reduce the impact from the remaining minor discrepancies, we built the bias
320 correction function daily to obtain bias for each sounding via interpolation of the continuum level radiance (Sun et al., 2017b,
321 2018).

322 The bias curves shown in Figure 2 differ significantly between TanSat and OCO-2. This is mostly due to the differences in
323 instrument performance and radiometric calibration. In general, the TanSat bias curves exhibited two peaks at radiance levels
324 of approximately 40 and 125 $\text{W m}^{-2} \mu\text{m}^{-1} \text{ sr}^{-1}$, separately, and most biases were larger than 0.015. For OCO-2, the curves
325 dropped sharply at low radiance levels, reaching the valley at a radiance level of approximately 40 $\text{W m}^{-2} \mu\text{m}^{-1} \text{ sr}^{-1}$, and then
326 increased slowly with the radiance level.

删除的内容: list in the retrieval

删除的内容: of

删除的内容: for surface pressure correction

删除的内容: Unlike

删除的内容: radiation

删除的内容: transmission

删除的内容: in inversion

带格式的: 非突出显示

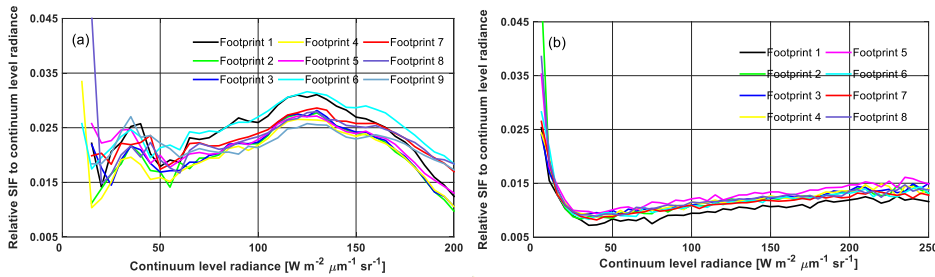
删除的内容: In the retrieval, a continuum level radiance bin fit was used to estimate the bias. The bins have a continuum level radiance interval of $5 \text{ W m}^{-2} \mu\text{m}^{-1} \text{ sr}^{-1}$. In each bin, the mean bias was estimated using all non-fluorescence measurements, and a piecewise linear function was built from the mean bias of each continuum level radiance interval.

带格式的: 突出显示

带格式的: 突出显示

删除的内容: se

删除的内容: retrieved



342
343 **Figure 2: Variations in the bias correction curves of continuum level radiance from (a) TanSat on July 7, 2017, and (b) Orbiting**
344 **Carbon Observatory-2 (OCO-2) on June 16, 2017. The different colors in the legend present different footprints of the satellite frame.**

345 2.3 Data Quality Controls

346 Only data that passed quality control were used in further applications. There were two data quality control processes for the
347 SIF products: pre-screening and post-screening. Pre-screening focused mainly on cloud screening; only cloud-free
348 measurements were used in SIF retrieval. A surface pressure difference (SPD), defined as:

$$349 \Delta P_0 = |P_{retrieval} - P_{ECMWF}| \quad (3)$$

350 was used to evaluate cloud contamination along with a chi-square test

$$351 \chi^2 = \sum \frac{(y_{sim} - y_{obs})^2}{y_{noise}^2} \quad (4)$$

352 where y_{sim} , y_{obs} , and y_{noise} represent the model fitting spectrum, observation spectrum, and spectrum noise, respectively.

353 $P_{retrieval}$ is the apparent surface pressure obtained from O₂-A band surface pressure retrieval, assuming a Rayleigh scattering
354 atmosphere. P_{ECMWF} is the surface pressure data from the ECMWF interim (0.75° × 0.75°) reanalysis data product (Dee et al.,
355 2011) which is interpolated to the sounding location and corrected for elevation differences with the Shuttle Radar Topography
356 Mission Global 30 Arc-Second Elevation digital elevation model (DOI: 10.5067/MEaSURES/SRTM/SRTMGL30.002). A
357 “cloud-free” measurement was required to simultaneously satisfy an SPD of less than 20 hPa and a χ^2 value of less than 80.
358 Here, post-screening was applied to filter out “bad” retrievals; this screening process involved the following steps: (1) SIF
359 retrievals with reduced χ^2 (χ_{red}^2) values ranging from 0.7 to 1.3 were considered “good” fitting, (2) continuum level radiance
360 outside the range of 15 ~ 200 W m⁻² μm⁻¹ sr⁻¹ was screened out to avoid scenes too bright or too dark, and (3) soundings with
361 the SZA higher than 60° were also filtered out.

362 带格式的: 英语 (英国)

363 2.4 IAPCAS versus IMAP-DOAS OCO-2 SIF Retrieval

364 Before applied to TanSat retrievals, we tested the IAPCAS/SIF algorithm on the OCO-2 L1B data first
365 (OCO2_L1B_Science.8r) and then compared the retrieval results with the OCO-2 L2 Lite SIF product (OCO2_Level

删除的内容: single

删除的内容:

带格式的: 非突出显示

带格式的: 非突出显示

删除的内容: surface pressure

带格式的: 突出显示

369 2_Lite_SIF.8r) retrieved by the Iterative Maximum A Posteriori-Differential Optical Absorption Spectroscopy (IMAP-DOAS)
 370 algorithm (Frankenberg, 2014b). The Lite product provides the SIF value for each sounding and hence the SIF comparison
 371 could be performed on the sounding scale for each month.

删除的内容: on a daily basis

372 Table 1 displays the relationship of OCO-2 SIF values between the IAPCAS/SIF and IMAP-DOAS at 757 nm micro-window
 373 for each month. Overall, the two SIF products were in good agreement. The linear fitting of the two SIF products suggests that
 374 they are highly correlated, as indicated by the strong linear relationship with R^2 mostly larger than 0.85 and the root mean
 375 square error (RMSE) of about $0.2 \text{ W m}^{-2} \mu\text{m}^{-1} \text{ sr}^{-1}$. Good consistency between the two SIF products implies the reliability of
 376 the IAPCAS/SIF algorithm; thus, it was further applied to TanSat SIF retrieval. However, there was still a small bias in the
 377 comparisons, which was due, most likely, to the impact of differences in the bias correction method, retrieval algorithm, and
 378 fitting window.

379 **Table 1:** Summary of the relationship between the IAPCAS,OCO-2 and IMAP-DOAS,OCO-2 solar-induced chlorophyll fluorescence
 380 (SIF) products at 757nm micro-window.

month	Number of soundings	Slope	Intercept	R^2	RMSE/ $\text{W m}^{-2} \mu\text{m}^{-1} \text{ sr}^{-1}$
2017/03	1097277	0.85	0.034	0.86	0.18
2017/04	1119464	0.86	0.045	0.87	0.19
2017/05	1054235	0.88	0.041	0.88	0.19
2017/06	1014848	0.91	0.032	0.90	0.19
2017/07	965309	0.92	0.011	0.91	0.19
2017/09	211219	0.88	0.005	0.81	0.23
2017/10	473359	0.88	0.031	0.88	0.17
2017/11	579009	0.87	0.022	0.85	0.19
2017/12	645134	0.87	0.020	0.88	0.16
2018/01	788655	0.87	0.019	0.88	0.17
2018/02*	629995	0.86	0.024	0.87	0.18

删除的内容: Institute of Atmospheric Physics Carbon Dioxide Retrieval Algorithm for Satellite Remote Sensing (

删除的内容:)

删除的内容: Iterative Maximum A Posteriori-Differential Optical Absorption Spectroscopy (

删除的内容:)

381 * Due to the lack of OCO-2 measurements in August 2017, the comparison is only performed for 11 months.

382 3 Results and Discussion

383 3.1 Comparison between TanSat and OCO-2 SIF Measurements

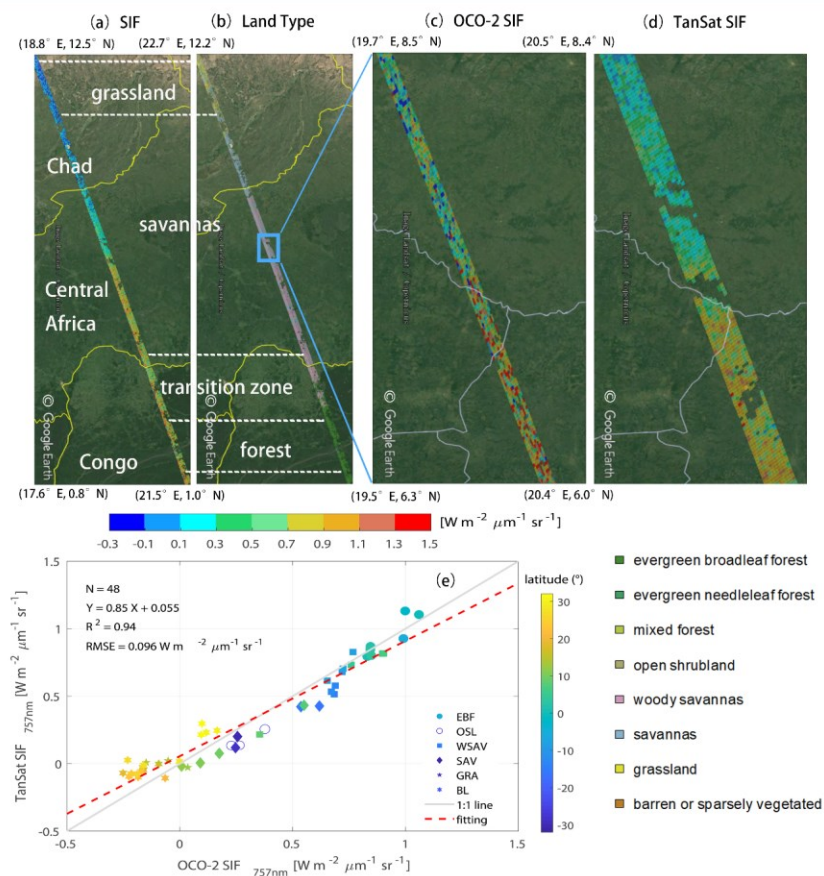
384 The comparison between TanSat and OCO-2 SIF measurements is a useful and powerful method for further verification of the
 385 IAPCAS/SIF algorithm. The reason for adopting OCO-2 data is that OCO-2 and TanSat have similar observation modes,
 386 including scanning method, transit time, spatial resolution, spectral resolution, and spectral range. The similarities mean that
 387 the SIF product from the two satellite missions can be directly compared. Directly comparing OCO-2 and TanSat SIF
 388 measurements could provide information on joint data application at the sounding scale for further studies. However, an
 389 identical sounding overlap barely exists because the two satellites often have different nadir tracks on the ground, which is
 390 induced by the different temporal and spatial intervals of the two satellite missions. Fortunately, the ground tracks of the two

删除的内容: Measurements

399 satellites were relatively close from April 17 to April 23, 2017. A couple of overlapping orbits were found in the measurements
400 obtained from Africa with the orbit number of 1733 from TanSat and 14890a from OCO-2 (Figure 3). In the comparison, the
401 OCO2_Level 2_Lite_SIF.8r product was used to present the SIF emission over the study area. These overlapping
402 measurements encompassed multiple land cover types, in which the SIF varied within an acceptable time difference (<5 min).
403 Overall, measurements from the two satellites indicated SIF variation with land cover type. The SIF emission over evergreen
404 broadleaf forests was larger than that over savannas, and grasslands exhibited the lowest SIF emission in April (Figure 3a,b).
405 The mean SIF emission over evergreen broadleaf forests was approximately $0.9\text{-}1.1 \text{ W m}^{-2} \mu\text{m}^{-1} \text{ sr}^{-1}$, whereas those over
406 savannas and grasslands were $0.5\text{-}0.7 \text{ W m}^{-2} \mu\text{m}^{-1} \text{ sr}^{-1}$ and less than $0.1 \text{ W m}^{-2} \mu\text{m}^{-1} \text{ sr}^{-1}$, respectively (Figure 3c,d).
407 Furthermore, we also found a significant difference in the SIF emission intensity over tropical savannas, which was observed
408 by both satellites (Figure 3c,d).

409

410



411

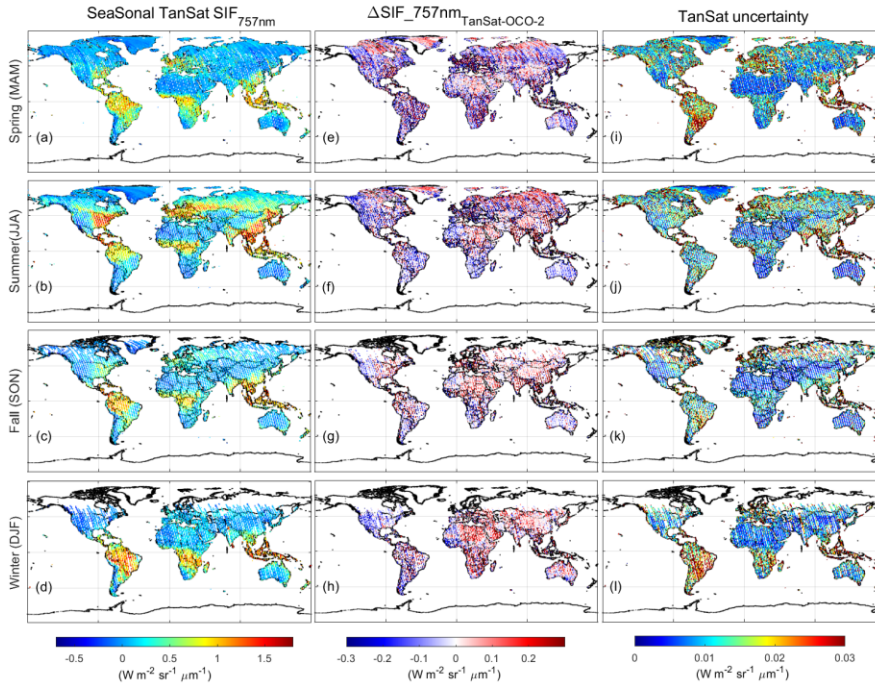
412 **Figure 3: Overlapping orbits of TanSat and OCO-2 on April 19, 2017 over Africa displayed in Google Earth, (a) the SIF**
 413 **measurements from both satellites and (b) the footprint land cover type were compared. Compared to OCO-2, TanSat has a wider**
 414 **swath width. A zoom-in view over savannas shows variations in the SIF signal measured by (c) OCO-2 and (d) TanSat. The land**
 415 **surface image shown in Google earth is provided by Landsat/Copernicus team. Following the International Geosphere-Biosphere**
 416 **Programme classification scheme, the vertical legend on the bottom right corner depicts the land cover type that occurs in the study**
 417 **area. The middle horizontal color bar represents the intensity of the SIF radiance. (e) Small-area SIF comparison between OCO-2**
 418 **and TanSat; each data point represents the mean SIF of a degree in latitude (colors) along the track. The marker legend that is**
 419 **shown on the bottom right of the plot indicates the dominant land cover (defined as the majority land cover type of each sounding)**
 420 **in each small area. There are six land cover types including evergreen broadleaf forest (EBF), open shrubland (OSL), woody savanna**
 421 **(WSAV), savanna (SAV), grassland (GRA), and barren land (BL). The red dashed line represents the linear fit between the two SIF**
 422 **products with statistics shown in the upper left of the plot. The gray line indicates a 1:1 relationship for reference.**

删除的内容: the two

424

425 Because the footprint sizes of the two satellites are different, it is difficult to make a direct footprint-to-footprint comparison.
426 Therefore, we made the comparison between the two satellite measurements based on a small area average. Each small area
427 spans a degree in latitude and continues along the track. The small area-averaged SIF comparison is shown in Figure 3e. The
428 results indicate good agreement, with an R^2 of 0.94 and an RMSE of $0.096 \text{ W m}^{-2} \mu\text{m}^{-1} \text{ sr}^{-1}$. Additional ground-based SIF
429 measurement setups (Guanter et al., 2007; Liu et al., 2019; van der Tol et al., 2016; Yang et al., 2015a; Yu et al., 2019) should
430 allow for direct evaluation of satellite retrieval accuracy in the future.

431



432

433 **Figure 4: Global TanSat SIF (left, a-d), differences between TanSat and IAPCAS OCO-2 SIF values (middle, e-h), and the grid-cell**
434 **retrieval uncertainty estimated from TanSat (right, i-l) at $1^\circ \times 1^\circ$ spatial resolution. The maps in each row represent a Northern**
435 **Hemisphere season, i.e., spring (MAM), summer (JJA), fall (SON), and winter (DJF).**

436

437 Figure 4 shows the global SIF comparison between IAPCAS/SIF retrieved from OCO-2 and TanSat; this comparison is only
 438 performed at $1^\circ \times 1^\circ$ spatial resolution. In general, the difference in SIF globally is mostly less than $0.3 \text{ W m}^{-2} \mu\text{m}^{-1} \text{ sr}^{-1}$ for
 439 all seasons, and on average, the smallest difference appears in fall. There are regional biases observed in North Africa, South
 440 Africa, South America, and Europe in all seasons except fall. This is mainly caused by the differences in instrument
 441 performance between TanSat and OCO-2, such as the Instrument Spectral Response and the Signal-to-Noise. The instrument
 442 performance difference is represented by the different structural characteristics of the bias curves. The bias correction
 443 compensates for most of the bias caused by instrument performance; however, small biases could remain. Furthermore, the
 444 hundreds of kilometers of distance between the OCO-2 and TanSat footprints, for example, over different vegetation regions,
 445 will also cause some measurement discrepancies. The global distribution of the two satellites was also compared with the
 446 official OCO-2 SIF data on the global scale, the results show that the difference between the retrieved SIF maps and the official
 447 map is less than $0.2 \text{ W m}^{-2} \mu\text{m}^{-1} \text{ sr}^{-1}$, indicating that the retrieved SIF data from OCO-2 and TanSat both have good SIF
 448 characterization capabilities on a global scale. The uncertainty σ of each sounding was estimated to validate SIF reliability and
 449 is provided in the product. σ is derived from the retrieval error covariance matrix, $S_e = (K^T S_0^{-1} K)^{-1}$, where K is the Jacobian
 450 matrix from the forward model fitting and S_0 is the measurement error covariance matrix that is calculated from the instrument
 451 spectrum noise. In general, σ ranges from 0.1 to $0.6 \text{ W m}^{-2} \mu\text{m}^{-1} \text{ sr}^{-1}$ for both TanSat and OCO-2 measurements in the 757
 452 nm fitting window, which is of a similar magnitude and data range as those of previous studies (Du et al., 2018; Frankenberg
 453 et al., 2014a). Meanwhile, the standard error of the mean SIF in each grid σ_{meas} was estimated to represent the gridded retrieval
 454 error and natural variability, which is calculated from TanSat SIF values with $\sigma_{meas} = \frac{\sigma_{std}}{\sqrt{n}}$ and $\sigma_{std} = \sqrt{\frac{\sum_{i=1}^n (SIF_i - \overline{SIF})^2}{n}}$, where
 455 σ_{std} represents the standard deviation of the grid cell with n soundings, SIF_i is the retrieved SIF values of each sounding,
 456 and \overline{SIF} is the mean SIF value for all measurements in the grid. As depicted in the right column of Figure 4, the σ_{meas} of each
 457 grid cell is much lower than the precision of a single sounding. The σ_{meas} for South America is larger than that for any other
 458 region on the globe (Figure 4i-l). This is similar to that of OCO-2 SIF retrieval and caused by fewer effective measurements
 459 due to the South Atlantic Anomaly (Sun et al., 2018). The difference in SIF emission values between the two satellites indicates
 460 that the synergistic use of two satellite SIF products still requires analysis of the impact of instrument differences, although
 461 the two satellite SIF products share the same spatiotemporal pattern on a global scale.

删除的内容: Function

带格式的: 非突出显示

462 3.2 SIF Global Distribution and Temporal Variation

463 The SIF emission intensity reflects the growth status of vegetation, and hence the overall global vegetation status can be
 464 represented by global SIF maps for each season. TanSat SIF over a whole year's cycle, from March 2017 to February 2018, is
 465 represented seasonally as a $1^\circ \times 1^\circ$ grid spatially. The seasonal variation in SIF emission is clear in the Northern Hemisphere,
 466 i.e., it is enhanced from spring to summer and then decreases (Sun et al., 2018).

删除的内容: due to its correlation with photosynthetic efficiency

删除的内容: ;

删除的内容: ,

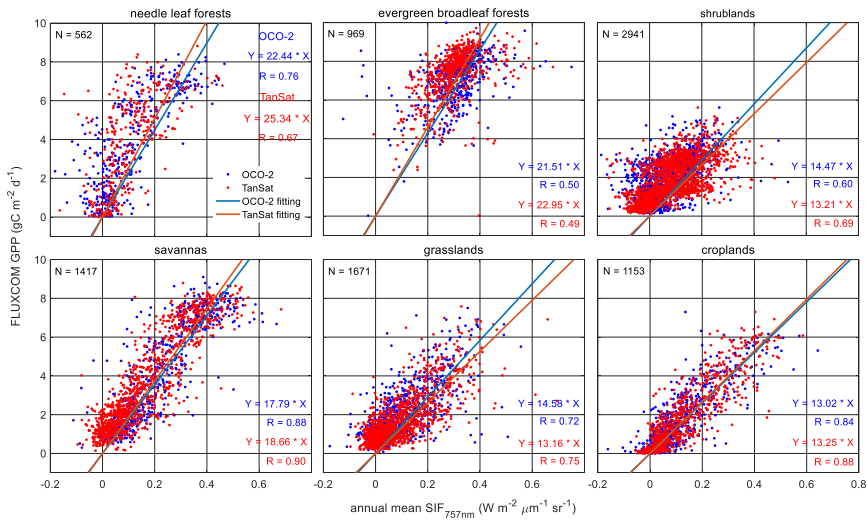
467 In general, the SIF emission varied with latitude and the vegetation-covered areas near the equator maintained a continuous
 468 SIF emission throughout the year. Large SIF emissions in the Northern Hemisphere, above $1.5 \text{ W m}^{-2} \mu\text{m}^{-1} \text{ sr}^{-1}$, mostly from

474 the eastern U.S., southeast of China, and southern Asia in summer, were due to the large areas of cropland. There was also an
 475 obvious SIF emission of 1-1.2 W m⁻² μm⁻¹ sr⁻¹ observed over Central Europe and northeastern China during the summer. In
 476 these regions, croplands and deciduous forests contribute to SIF emissions. In the Southern Hemisphere, the strongest SIF
 477 emission occurred in the Amazon, with a level of approximately 1-2 W m⁻² μm⁻¹ sr⁻¹ in DJF (Northern Hemisphere winter),
 478 where there is an evergreen broadleaf rainforest. Africa, which is covered by evergreen broadleaf rainforests and woody
 479 savannas, had an average SIF value of 0.7-1.5 W m⁻² μm⁻¹ sr⁻¹ during the year.

480 The SIF-GPP relationship over different vegetation types was also investigated by comparing the annual mean satellite SIF
 481 measurements with the FLUXCOM GPP (Jung et al., 2020; Tramontana et al., 2016) dataset in a 1° × 1° grid over the globe.
 482 The FLUXCOM GPP dataset used in the study comprises monthly global gridded flux products with remote sensing and
 483 meteorological/climate forcing (RS+METEO) setups, which are derived from mean seasonal cycles according to MODIS data
 484 and daily meteorological information (Jung et al., 2020; Tramontana et al., 2016). In the correlation analysis, the high spatial
 485 resolution (0.5° × 0.5°) of the FLUXCOM GPP was first resampled to 1° × 1° to keep the same temporal-spatial scale of SIF
 486 and GPP data. The satellite-measured SIF is an instantaneous emission signal that varies with incident solar radiance within
 487 the day. To reduce the differences caused by the observation time and SZA at different latitudes, we applied a daily adjustment
 488 factor to convert the instantaneous SIF emission into a daily mean SIF (Du et al., 2018; Frankenberg et al., 2011b; Sun et al.,
 489 2018). The daily adjustment factor d is calculated as follows:

$$490 \quad d = \frac{\int_{t=t_0-12h}^{t=t_0+12h} \cos(SZA(t)) \cdot dt}{\cos(SZA(t_0))} \quad (5)$$

491 where t_0 is the observation time in fractional days and $SZA(t)$ is a function of latitude, longitude, and time for calculating the
 492 SZA of the measurements. The annual averaged SIF is calculated from the daily mean SIF. To evaluate the relationship
 493 between SIF and GPP on the periodic scale of vegetation growth status, annually-averaged data were used in the regression
 494 fitting analysis.



495

496 **Figure 5: Relationship between annual mean SIF and FLUXCOM gross primary production (GPP) from March 2017 to February**
 497 **2018. Blue and red dots represent OCO-2 and TanSat SIF grids, respectively. Fitted lines and statistics for OCO-2 and TanSat**
 498 **are shown in each plot.**

499 Figure 5 shows the linear fits for six vegetation types, including needle leaf forest, evergreen broadleaf forest, shrubland,
 500 savanna, grassland, and cropland. Recent studies have shown a strong linear correlation between SIF and GPP. The TanSat
 501 SIF and the OCO-2 official SIF data were used to estimate the SIF-GPP correlation. To make a direct comparison of the
 502 relationship between SIF and GPP among various vegetation types, we used non-offset linear fitting to indicate the correlation
 503 between satellite SIF and FLUXCOM GPP. For savanna and cropland, there were strong relationships between the mean SIF
 504 and GPP with an R-value above 0.84. The fitting results show that the SIF products of the two satellites have similar capabilities
 505 in characterizing GPP, especially for the evergreen broadleaf forest, savanna, and cropland, with slopes of approximately 21,
 506 18, and 13, respectively. For shrubland and grassland, the slope of OCO-2 SIF with GPP is higher than that of TanSat and has
 507 a worse correlation. For forests, OCO-2 SIF presents a better correlation with GPP, especially in the needle leaf forest. As a
 508 whole, for the same vegetation type, the SIF-GPP correlations for the two satellites are rather similar, indicating that the two
 509 satellite SIF products have similar capabilities in characterizing GPP. It shows the strong feasibility of the comprehensive
 510 application of different satellite SIF products. For different vegetation types, the SIF-GPP correlations were significantly
 511 different, indicating the different ability of SIF to characterize GPP of different vegetation. It represents that vegetation type
 512 is a key factor in determining the SIF-GPP relationship. The markedly different fitting slopes across various biomes suggest
 513 that the application of SIF in GPP estimation needs more detailed analysis although the evidence of the strong linear
 514 relationship between them.

515 4 Conclusions

516 In this paper, we introduced the retrieval algorithm IAPCAS/SIF and its application in TanSat and OCO-2 measurements. One
517 year (March 2017-February 2018) of TanSat SIF data was introduced and compared with OCO-2 measurements in this study.
518 The TanSat and OCO-2 SIF products based on the IAPCAS/SIF algorithm are available on the Cooperation on the Analysis
519 of carbon SATellites data (CASA) website, www.chinageoss.org/tansat. ~~Comparing~~ TanSat and OCO-2 measurements directly,
520 using a case study, and indirectly, with global $1^{\circ}\times 1^{\circ}$ grid data, showed consistency between the two satellite missions,
521 indicating that the coordinated usage of the two data products is possible in future studies. The correlation analysis between
522 SIF and GPP further verified the feasibility of the ~~synergistic~~ application of SIF products from different satellite missions.
523 Meanwhile, it should be noticed that the difference in the ability of satellite SIF products to characterize different vegetation
524 types in data applications. With ~~more~~ satellites becoming available for SIF observations, space-based SIF observations have
525 recently expanded in range to provide broad spatiotemporal coverage. The next-generation Chinese carbon monitoring satellite
526 (TanSat-2) is now in the preliminary design phase, which is designed to be a constellation of six satellites to measure different
527 kinds of greenhouse gases and trace gases in a more efficient way, including CO₂, CH₄, CO, NO_x, as well as SIF. SIF
528 measurements from TanSat-2 will provide global data products over broader coverage areas with less noise. The improvement
529 in the spatiotemporal resolution of SIF data will benefit GPP predictions based on the numerous studies of the linear
530 relationship between SIF and GPP. In future work, the measurement accuracy should be validated directly using ground-based
531 measurements to ensure data quality.

532 Data availability

533 The SIF products of TanSat and OCO-2 by IAPCAS/SIF algorithm are available on the Cooperation on the Analysis of carbon
534 SATellites data (CASA) website (<http://www.chinageoss.cn/tansat/index.html>).

536 Author contributions

537 L.Y. and D.Y. developed the retrieval algorithm, designed the study, and wrote the paper. Y.L. led the SIF data process and
538 analysis. Y.L., D.Y., Z.C., and J.W. contributed to manuscript organization and revision. C.L. and Y.Z. provided information
539 on the TanSat instrument performance. L.T. provided TanSat in-flight information. M.W. and S.W. provided information on
540 the scientific requirement for data further application. N.L. and D.L. led the TanSat data application. Z.Y. led the TanSat in-
541 flight operation.

刪除的內容: -

刪除的內容: Comparisons

刪除的內容: between

刪除的內容: comprehensive

刪除的內容: increasing

刪除的內容: www.chinageoss.org/tansat

548 Competing interests

549 The authors declare that they have no conflict of interest.

550 Acknowledgments

551 The TanSat L1B data service was provided by the International Reanalysis Cooperation on Carbon Satellites Data (IRCSD)
552 and the Cooperation on the Analysis of carbon Satellites data (CASA). The authors thank OCO-2 Team for providing Level-
553 1B data and Level-2 SIF data products. The authors thank the FLUXCOM team for providing global GPP data. The authors
554 thank Google for allowing free use of Google Earth and reproduction of maps for publication. The authors also thank the
555 Landsat/Copernicus team for providing land surface images for Google Earth.

556 Financial support

557 This work has been supported by the [National Key R&D Program of China \(Grant No. 2021YFB3901000\)](#), the Key Research
558 Program of the Chinese Academy of Sciences (ZDRW-ZS-2019-1), and the Youth Program of the National Natural Science
559 Foundation of China ([Grant No. 41905029](#), [Grant No. 42105113](#)).

560 References

- 561 [Bösch, H., Toon, G. C., Sen, B., Washenfelder, R. A., Wennberg, P. O., Buchwitz, M., de Beek, R., Burrows, J. P., Crisp, D.,](#)
562 [Christi, M., Connor, B. J., Natraj, V., and Yung, Y. L.: Space-based near-infrared CO₂ measurements: Testing the Orbiting](#)
563 [Carbon Observatory retrieval algorithm and validation concept using SCIAMACHY observations over Park Falls, Wisconsin,](#)
564 [J. Geophys. Res. Atmos., 111, 1–17, <https://doi.org/10.1029/2006JD007080>, 2006.](#)
565 [Cai, Z. N., Liu, Y., and Yang, D. X.: Analysis of XCO₂ retrieval sensitivity using simulated Chinese Carbon Satellite \(TanSat\)](#)
566 [measurements, Sci. China Earth Sci., 57, 1919–1928, <https://doi.org/10.1007/s11430-013-4707-1>, 2014.](#)
567 [Chen, A., Mao, J., Ricciuto, D., Xiao, J., Frankenberg, C., Li, X., Thornton, P. E., Gu, L., and Knapp, A. K.: Moisture](#)
568 [availability mediates the relationship between terrestrial gross primary production and solar-induced chlorophyll fluorescence:](#)
569 [Insights from global-scale variations, Glob. Chang. Biol., 1–13, <https://doi.org/10.1111/gcb.15373>, 2020.](#)
570 [Dee, D. P., Uppala, S. M., Simmons, A. J., Berrisford, P., Poli, P., Kobayashi, S.: The ERA - interim reanalysis: Configuration](#)
571 [and performance of the data assimilation system. Q. J. R. Meteorol. Soc., 137\(656\), 553–597, <https://doi.org/10.1002/qj.828>,](#)
572 [2011.](#)
573 [Doughty, R., Köhler, P., Frankenberg, C., Magney, T. S., Xiao, X., Qin, Y., Wu, X., and Moore, B.: TROPOMI reveals dry-](#)
574 [season increase of solar-induced chlorophyll fluorescence in the Amazon forest, Proc. Natl. Acad. Sci. U. S. A., 116, 22393–](#)
575 [22398, <https://doi.org/10.1073/pnas.1908157116>, 2019.](#)

删除的内容: 3

带格式的: 字体: (中文) Times New Roman, 10 磅

带格式的: 字体: (中文) Times New Roman, 10 磅

删除的内容: Boesche, E., Stammes, P., and Bennartz, R.: Aerosol influence on polarization and intensity in near-infrared O₂ and CO₂ absorption bands observed from space, J. Quant. Spectrosc. Radiat. Transf., 110, 223–239, <https://doi.org/10.1016/j.jqsrt.2008.09.019>, 2009.

删除的内容: .

删除的内容: Butz, A., Guerlet, S., Hasekamp, O., Schepers, D., Galli, A., Aben, I., Frankenberg, C., Hartmann, J. M., Tran, H., Kuze, A., Keppel-Aleks, G., Toon, G., Wunch, D., Wennberg, P., Deutscher, N., Griffith, D., Macatangay, R., Messerschmidt, J., Notholt, J., and Warneke, T.: Toward accurate CO₂ and CH₄ observations from GOSAT, Geophys. Res. Lett., 38, 2–7, <https://doi.org/10.1029/2011GL047888>, 2011. .
Butz, A., Hasekamp, O. P., Frankenberg, C., and Aben, U.: Retrievals of atmospheric CO₂ from simulated space-borne measurements of backscattered near-infrared sunlight: Accounting for aerosol effects, Appl. Opt., 48, 3322–3336, <https://doi.org/10.1364/AO.48.003322>, 2009. .
Butz, A., Hasekamp, O. P., Frankenberg, C., Vidot, J., and Aben, I.: CH₄ retrievals from space-based solar backscatter measurements: Performance evaluation against simulated aerosol and cirrus loaded scenes, J. Geophys. Res. Atmos., 115, 1–15, <https://doi.org/10.1029/2010JD014514>, 2010. .

600 Drusch, M., Moreno, J., del Bello, U., Franco, R., Goulas, Y., Huth, A., Kraft, S., Middleton, E. M., Miglietta, F., Mohammed,
601 G.: The FLuorescence EXplorer Mission Concept—ESA’s Earth Explorer 8, ITGRS, 55, 1273–1284,
602 <http://doi.org/10.1109/TGRS.2016.2621820>, 2017.

603 Du, S., Liu, L., Liu, X., Zhang, X., Zhang, X., Bi, Y., and Zhang, L.: Retrieval of global terrestrial solar-induced chlorophyll
604 fluorescence from TanSat satellite, *Sci. Bull.*, 63, 1502–1512, <https://doi.org/10.1016/j.scib.2018.10.003>, 2018.

605 Frankenberg, C., Butz, A., and Toon, G. C.: Disentangling chlorophyll fluorescence from atmospheric scattering effects in O2
606 A-band spectra of reflected sunlight, *Geophys. Res. Lett.*, 38, 1–5, <https://doi.org/10.1029/2010GL045896>, 2011a.

607 Frankenberg, C., Fisher, J. B., Worden, J., Badgley, G., Saatchi, S. S., Lee, J. E., Toon, G. C., Butz, A., Jung, M., Kuze, A.,
608 and Yokota, T.: New global observations of the terrestrial carbon cycle from GOSAT: Patterns of plant fluorescence with gross
609 primary productivity, *Geophys. Res. Lett.*, 38, 1–6, <https://doi.org/10.1029/2011GL048738>, 2011b.

610 Frankenberg, C., O’Dell, C., Berry, J., Guanter, L., Joiner, J., Köhler, P., Pollock, R., and Taylor, T. E.: Prospects for
611 chlorophyll fluorescence remote sensing from the Orbiting Carbon Observatory-2, *Remote Sens. Environ.*, 147, 1–12,
612 <https://doi.org/10.1016/j.rse.2014.02.007>, 2014a.

613 Frankenberg, C., O’Dell, C., Guanter, L., and McDuffie, J.: Remote sensing of near-infrared chlorophyll fluorescence from
614 space in scattering atmospheres: Implications for its retrieval and interferences with atmospheric CO₂ retrievals, *Atmos. Meas.*
615 *Tech.*, 5, 2081–2094, <https://doi.org/10.5194/amt-5-2081-2012>, 2012.

616 Frankenberg, C.: OCO-2 Algorithm Theoretical Basis Document: IMAP-DOAS pre-processor, 2014b.

617 Guanter, L., Aben, I., Tol, P., Krijger, J. M., Hollstein, A., Köhler, P., Damm, A., Joiner, J., Frankenberg, C., and Landgraf,
618 J.: Potential of the TROPOspheric Monitoring Instrument (TROPOMI) onboard the Sentinel-5 Precursor for the monitoring
619 of terrestrial chlorophyll fluorescence, <https://doi.org/10.5194/amt-8-1337-2015>, 2015.

620 Guanter, L., Alonso, L., Gómez-Chova, L., Amorós-López, J., Vila, J., and Moreno, J.: Estimation of solar-induced vegetation
621 fluorescence from space measurements, *Geophys. Res. Lett.*, 34, 1–5, <https://doi.org/10.1029/2007GL029289>, 2007.

622 Guanter, L., Frankenberg, C., Dudhia, A., Lewis, P. E., Gómez-Dans, J., Kuze, A., Suto, H., and Grainger, R. G.: Retrieval
623 and global assessment of terrestrial chlorophyll fluorescence from GOSAT space measurements, *Remote Sens. Environ.*, 121,
624 236–251, <https://doi.org/10.1016/j.rse.2012.02.006>, 2012.

625 Guanter, L., Zhang, Y., Jung, M., Joiner, J., Voigt, M., Berry, J. A., Frankenberg, C., Huete, A. R., Zarco-Tejada, P., Lee, J.
626 E., Moran, M. S., Ponce-Campos, G., Beer, C., Camps-Valls, G., Buchmann, N., Gianelle, D., Klumpp, K., Cescatti, A., Baker,
627 J. M., and Griffiths, T. J.: Global and time-resolved monitoring of crop photosynthesis with chlorophyll fluorescence, *Proc. Natl.*
628 *Acad. Sci. U. S. A.*, 111, <https://doi.org/10.1073/pnas.1320008111>, 2014.

629 Joiner, J., Guanter, L., Lindstrot, R., Voigt, M., Vasilkov, A. P., Middleton, E. M., Huemmrich, K. F., Yoshida, Y., and
630 Frankenberg, C.: Global monitoring of terrestrial chlorophyll fluorescence from moderate-spectral-resolution near-infrared
631 satellite measurements: methodology, simulations, and application to GOME-2, *Atmos. Meas. Tech.*, 6, 2803–2823,
632 <https://doi.org/10.5194/amt-6-2803-2013>, 2013.

633 Joiner, J., Yoshida, Y., Guanter, L., and Middleton, E. M.: New methods for the retrieval of chlorophyll red fluorescence from
634 hyperspectral satellite instruments: simulations and application to GOME-2 and SCIAMACHY, *Atmos. Meas. Tech.*, 9, 3939–
635 3967, <https://doi.org/10.5194/amt-9-3939-2016>, 2016.

636 Joiner, J., Yoshida, Y., Vasilkov, A. P., Middleton, E. M., Campbell, P. K. E., Yoshida, Y., Kuze, A., and Corp, L. A.: Filling-
637 in of near-infrared solar lines by terrestrial fluorescence and other geophysical effects: simulations and space-based
638 observations from SCIAMACHY and GOSAT, *Atmos. Meas. Tech.*, 5, 809–829, <https://doi.org/10.5194/amt-5-809-2012>,
639 2012.

640 Joiner, J., Yoshida, Y., Vasilkov, A. P., Yoshida, Y., Corp, L. A., and Middleton, E. M.: First observations of global and
641 seasonal terrestrial chlorophyll fluorescence from space, 8, 637–651, <https://doi.org/10.5194/bg-8-637-2011>, 2011.

642 Joiner, J., Yoshida, Y., Zhang, Y., Duveiller, G., Jung, M., Lyapustin, A., Wang, Y., and Tucker, C. J.: Estimation of terrestrial
643 global gross primary production (GPP) with satellite data-driven models and eddy covariance flux data, *Remote Sens.*, 10, 1–
644 38, <https://doi.org/10.3390/rs10091346>, 2018.

645 Jung, M., Schwalm, C., Migliavacca, M., Walther, S., Camps-Valls, G., Koirala, S., Anthoni, P., Besnard, S., Bodesheim, P.,
646 Carvalhais, N., Chevallier, F., Gans, F., S Goll, D., Haverd, V., Köhler, P., Ichii, K., K Jain, A., Liu, J., Lombardozi, D., E
647 M S Nabel, J., A Nelson, J., O’Sullivan, M., Pallandt, M., Papale, D., Peters, W., Pongratz, J., Rödenbeck, C., Sitch, S.,
648 Tramontana, G., Walker, A., Weber, U., and Reichstein, M.: Scaling carbon fluxes from eddy covariance sites to globe:
649 Synthesis and evaluation of the FLUXCOM approach, 17, 1343–1365, <https://doi.org/10.5194/bg-17-1343-2020>, 2020.

650 Köhler, P., Frankenberg, C., Magney, T. S., Guanter, L., Joiner, J., and Landgraf, J.: Global Retrievals of Solar-Induced
651 Chlorophyll Fluorescence With TROPOMI: First Results and Intersensor Comparison to OCO-2, *Geophys. Res. Lett.*, 45,
652 10,456–10,463, <https://doi.org/10.1029/2018GL079031>, 2018b.

653 Köhler, P., Guanter, L., and Joiner, J.: A linear method for the retrieval of sun-induced chlorophyll fluorescence from GOME-
654 2 and SCIAMACHY data, *Atmos. Meas. Tech.*, 8, 2589–2608, <https://doi.org/10.5194/amt-8-2589-2015>, 2015.

655 Köhler, P., Guanter, L., Kobayashi, H., Walther, S., and Yang, W.: Assessing the potential of sun-induced fluorescence and
656 the canopy scattering coefficient to track large-scale vegetation dynamics in Amazon forests, *Remote Sens. Environ.*, 204,
657 769–785, <https://doi.org/10.1016/j.rse.2017.09.025>, 2018a.

658 Lee, J. E., Frankenberg, C., Van Der Tol, C., Berry, J. A., Guanter, L., Boyce, C. K., Fisher, J. B., Morrow, E., Worden, J. R.,
659 Asefi, S., Badgley, G., and Saatchi, S.: Forest productivity and water stress in Amazonia: Observations from GOSAT
660 chlorophyll fluorescence, *Tohoku J. Exp. Med.*, 230, <https://doi.org/10.1098/rspb.2013.0171>, 2013.

661 Li, X., Xiao, J., and He, B.: Chlorophyll fluorescence observed by OCO-2 is strongly related to gross primary productivity
662 estimated from flux towers in temperate forests, *Remote Sens. Environ.*, 204, 659–671,
663 <https://doi.org/10.1016/j.rse.2017.09.034>, 2018.

664 Li, X., Xiao, J., Kimball, J. S., Reichle, R. H., Scott, R. L., Litvak, M. E., Bohrer, G., and Frankenberg, C.: Synergistic use of
665 SMAP and OCO-2 data in assessing the responses of ecosystem productivity to the 2018 U.S. drought, *Remote Sens. Environ.*,
666 251, 112062, <https://doi.org/10.1016/j.rse.2020.112062>, 2020.

667 Liu, X., Guanter, L., Liu, L., Damm, A., Malenovsky, Z., Rascher, U., Peng, D., Du, S., and Gastellu-Etchegorry, J. P.:
668 Downscaling of solar-induced chlorophyll fluorescence from canopy level to photosystem level using a random forest model,
669 Remote Sens. Environ., 231, 110772, <https://doi.org/10.1016/j.rse.2018.05.035>, 2019.

670 Liu, Y., Wang, J., Yao, L., Chen, X., Cai, Z., Yang, D., Yin, Z., Gu, S., Tian, L., Lu, N., and Lyu, D.: The TanSat mission:
671 preliminary global observations, Sci. Bull., 63, 1200–1207, <https://doi.org/10.1016/j.scib.2018.08.004>, 2018.

672 MacBean, N., Maignan, F., Bacour, C., Lewis, P., Peylin, P., Guanter, L., Köhler, P., Gómez-Dans, J., and Disney, M.: Strong
673 constraint on modelled global carbon uptake using solar-induced chlorophyll fluorescence data, Sci. Rep., 8, 1–12,
674 <https://doi.org/10.1038/s41598-018-20024-w>, 2018.

675 [NASA JPL. NASA Shuttle Radar Topography Mission Global 30 arc second \[Data set\]. NASA EOSDIS Land Processes](https://doi.org/10.5067/MEaSURES/SRTM/SRTMGL30.002)
676 [DAAC. Accessed 2022-02-27 from https://doi.org/10.5067/MEaSURES/SRTM/SRTMGL30.002, 2013.](https://doi.org/10.5067/MEaSURES/SRTM/SRTMGL30.002)

677 O'Dell, C. W., Connor, B., Bösch, H., O'Brien, D., Frankenberg, C., Castano, R., Christi, M., Eldering, D., Fisher, B., Gunson,
678 M., McDuffie, J., Miller, C. E., Natraj, V., Oyafuso, F., Polonsky, I., Smyth, M., Taylor, T., Toon, G. C., Wennberg, P. O.,
679 and Wunch, D.: The ACOS CO₂ retrieval algorithm-Part 1: Description and validation against synthetic observations, Atmos.
680 Meas. Tech., 5, 99–121, <https://doi.org/10.5194/amt-5-99-2012>, 2012.

681 Qiu, R., Han, G., Ma, X., Xu, H., Shi, T., and Zhang, M.: A comparison of OCO-2 SIF, MODIS GPP, and GOSIF data from
682 gross primary production (GPP) estimation and seasonal cycles in North America, Remote Sens., 12,
683 <https://doi.org/10.3390/rs12020258>, 2020.

684 Reuter, M., Buchwitz, M., Schneising, O., Heymann, J., Bovensmann, H., and Burrows, J. P.: A method for improved
685 SCIAMACHY CO₂ retrieval in the presence of optically thin clouds, Atmos. Meas. Tech., 3, 209–232,
686 <https://doi.org/10.5194/amt-3-209-2010>, 2010.

687 Sun, K., Liu, X., Nowlan, C. R., Cai, Z., Chance, K., Frankenberg, C., Lee, R. A. M., Pollock, R., Rosenberg, R., and Crisp,
688 D.: Characterization of the OCO-2 instrument line shape functions using on-orbit solar measurements, Atmos. Meas. Tech.,
689 10, 939–953, <https://doi.org/10.5194/amt-10-939-2017>, 2017b.

690 Sun, Y., Frankenberg, C., Jung, M., Joiner, J., Guanter, L., Köhler, P., and Magney, T.: Overview of Solar-Induced chlorophyll
691 Fluorescence (SIF) from the Orbiting Carbon Observatory-2: Retrieval, cross-mission comparison, and global monitoring for
692 GPP, Remote Sens. Environ., 209, 808–823, <https://doi.org/10.1016/j.rse.2018.02.016>, 2018.

693 Sun, Y., Frankenberg, C., Wood, J. D., Schimel, D. S., Jung, M., Guanter, L., Drewry, D. T., Verma, M., Porcar-Castell, A.,
694 Griffiths, T. J., Gu, L., Magney, T. S., Köhler, P., Evans, B., and Yuen, K.: OCO-2 advances photosynthesis observation from
695 space via solar-induced chlorophyll fluorescence, Science (80-.), 358, <https://doi.org/10.1126/science.aam5747>, 2017a.

696 Sun, Y., Fu, R., Dickinson, R., Joiner, J., Frankenberg, C., Gu, L., Xia, Y., and Fernando, N.: Drought onset mechanisms
697 revealed by satellite solar-induced chlorophyll fluorescence: Insights from two contrasting extreme events, J. Geophys. Res.
698 G Biogeosciences, 120, 2427–2440, <https://doi.org/10.1002/2015JG003150>, 2015.

699 Tramontana, G., Jung, M., Schwalm, C. R., Ichii, K., Camps-Valls, G., Ráduly, B., Reichstein, M., Arain, M. A., Cescatti, A.,
700 Kiely, G., Merbold, L., Serrano-Ortiz, P., Sickert, S., Wolf, S., and Papale, D.: Predicting carbon dioxide and energy fluxes
701 across global FLUXNET sites with regression algorithms, *13*, 4291–4313, <https://doi.org/10.5194/bg-13-4291-2016>, 2016.
702 van der Tol, C., Rossini, M., Cogliati, S., Verhoef, W., Colombo, R., Rascher, U., and Mohammed, G.: A model and
703 measurement comparison of diurnal cycles of sun-induced chlorophyll fluorescence of crops, *Remote Sens. Environ.*, *186*,
704 663–677, <https://doi.org/10.1016/j.rse.2016.09.021>, 2016.
705 Yang, D., Boesch, H., Liu, Y., Somkuti, P., Cai, Z., Chen, X., Di Noia, A., Lin, C., Lu, N., Lyu, D., Parker, R. J., Tian, L.,
706 Wang, M., Webb, A., Yao, L., Yin, Z., Zheng, Y., Deutscher, N. M., Griffith, D. W. T., Hase, F., Kivi, R., Morino, I., Notholt,
707 J., Ohyama, H., Pollard, D. F., Shiomi, K., Sussmann, R., Té, Y., Velazco, V. A., Warneke, T., and Wunch, D.: Toward High
708 Precision XCO₂ Retrievals From TanSat Observations: Retrieval Improvement and Validation Against TCCON
709 Measurements, *J. Geophys. Res. Atmos.*, *125*, 1–26, <https://doi.org/10.1029/2020JD032794>, 2020.
710 Yang, D., Liu, Y., Boesch, H., Yao, L., Di Noia, A., Cai, Z., Lu, N., Lyu, D., Wang, M., Wang, J., Yin, Z., and Zheng, Y.: A
711 New TanSat XCO₂ Global Product towards Climate Studies, *Adv. Atmos. Sci.*, *38*, 8–11, <https://doi.org/10.1007/s00376-020-020-0297-y>, 2021.
712
713 Yang, D., Liu, Y., Cai, Z., Chen, X., Yao, L., and Lu, D.: First Global Carbon Dioxide Maps Produced from TanSat
714 Measurements, *Adv. Atmos. Sci.*, *35*, 621–623, <https://doi.org/10.1007/s00376-018-7312-6>, 2018.
715 Yang, D., Liu, Y., Cai, Z., Deng, J., Wang, J., and Chen, X.: An advanced carbon dioxide retrieval algorithm for satellite
716 measurements and its application to GOSAT observations, *Sci. Bull.*, *60*, 2063–2066, <https://doi.org/10.1007/s11434-015-0953-2>, 2015b.
717
718 Yang, X., Tang, J., Mustard, J. F., Lee, J. E., Rossini, M., Joiner, J., Munger, J. W., Kornfeld, A., and Richardson, A. D.: Solar-
719 induced chlorophyll fluorescence that correlates with canopy photosynthesis on diurnal and seasonal scales in a temperate
720 deciduous forest, *Geophys. Res. Lett.*, *42*, 2977–2987, <https://doi.org/10.1002/2015GL063201>, 2015a.
721 Yao, L., Yang, D., Liu, Y., Wang, J., Liu, L., Du, S., Cai, Z., Lu, N., Lyu, D., Wang, M., Yin, Z., and Zheng, Y.: A New
722 Global Solar-induced Chlorophyll Fluorescence (SIF) Data Product from TanSat Measurements, *Adv. Atmos. Sci.*, *38*, 341–
723 345, <https://doi.org/10.1007/s00376-020-0204-6>, 2021.
724 Yin, Y., Byrne, B., Liu, J., Wennberg, P. O., Davis, K. J., Magney, T., Köhler, P., He, L., Jeyaram, R., Humphrey, V., Gerken,
725 T., Feng, S., Digangi, J. P., and Frankenberg, C.: Cropland Carbon Uptake Delayed and Reduced by 2019 Midwest Floods,
726 *AGU Adv.*, *1*, 1–15, <https://doi.org/10.1029/2019av000140>, 2020.
727 Yoshida, Y., Joiner, J., Tucker, C., Berry, J., Lee, J. E., Walker, G., Reichle, R., Koster, R., Lyapustin, A., and Wang, Y.: The
728 2010 Russian drought impact on satellite measurements of solar-induced chlorophyll fluorescence: Insights from modeling
729 and comparisons with parameters derived from satellite reflectances, *Remote Sens. Environ.*, *166*, 163–177,
730 <https://doi.org/10.1016/j.rse.2015.06.008>, 2015.
731 Yoshida, Y., Kikuchi, N., Morino, I., Uchino, O., Oshchepkov, S., Bril, A., Saeki, T., Schutgens, N., Toon, G. C., Wunch, D.,
732 Roehl, C. M., Wennberg, P. O., Griffith, D. W. T., Deutscher, N. M., Warneke, T., Notholt, J., Robinson, J., Sherlock, V.,

733 Connor, B., Rettinger, M., Sussmann, R., Ahonen, P., Heikkinen, P., Kyrö, E., Mendonca, J., Strong, K., Hase, F., Dohe, S.,
734 and Yokota, T.: Improvement of the retrieval algorithm for GOSAT SWIR XCO₂ and XCH₄ and their validation using TCCON
735 data, *Atmos. Meas. Tech.*, 6, 1533–1547, <https://doi.org/10.5194/amt-6-1533-2013>, 2013.
736 Yoshida, Y., Ota, Y., Eguchi, N., Kikuchi, N., Nobuta, K., Tran, H., Morino, I., and Yokota, T.: Retrieval algorithm for CO₂
737 and CH₄ column abundances from short-wavelength infrared spectral observations by the Greenhouse gases observing satellite,
738 *Atmos. Meas. Tech.*, 4, 717–734, <https://doi.org/10.5194/amt-4-717-2011>, 2011.
739 Yu, L., Wen, J., Chang, C. Y., Frankenberg, C., and Sun, Y.: High-Resolution Global Contiguous SIF of OCO-2, *Geophys.*
740 *Res. Lett.*, 46, 1449–1458, <https://doi.org/10.1029/2018GL081109>, 2019.
741 Zhang, Y., Guanter, L., Berry, J. A., Joiner, J., van der Tol, C., Huete, A., Gitelson, A., Voigt, M., and Köhler, P.: Estimation
742 of vegetation photosynthetic capacity from space-based measurements of chlorophyll fluorescence for terrestrial biosphere
743 models, *Glob. Chang. Biol.*, 20, 3727–3742, <https://doi.org/10.1111/gcb.12664>, 2014.
744 Zhang, Y., Xiao, X., Zhang, Y., Wolf, S., Zhou, S., Joiner, J., Guanter, L., Verma, M., Sun, Y., Yang, X., Paul-Limoges, E.,
745 Gough, C. M., Wohlfahrt, G., Gioli, B., van der Tol, C., Yann, N., Lund, M., and de Grandcourt, A.: On the relationship
746 between sub-daily instantaneous and daily total gross primary production: Implications for interpreting satellite-based SIF
747 retrievals, *Remote Sens. Environ.*, 205, 276–289, <https://doi.org/10.1016/j.rse.2017.12.009>, 2018.

带格式的：正文

删除的内容： .

-
-
-

带格式的：英语(英国)